JGR Atmospheres

RESEARCH ARTICLE
10.1029/2021JD034574

Special Section:
Southern Ocean clouds, aerosols, precipitation and radiation

Ice in Southern Ocean Clouds With Cloud Top Temperatures Exceeding −5°C

Troy J. Zaremba[1], Robert M. Rauber[1], Greg M. McFarquhar[2,3], Paul J. DeMott[4], John J. D'Alessandro[2,3], and Wei Wu[2,3]

[1]Department of Atmospheric Sciences, University of Illinois at Urbana-Champaign, Urbana, IL, USA, [2]Cooperative Institute for Mesoscale and Microscale Studies, University of Oklahoma, Norman, OK, USA, [3]School of Meteorology, University of Oklahoma, Norman, OK, USA, [4]Department of Atmospheric Science, Colorado State University, Fort Collins, CO, USA

Abstract This study documents the presence of ice in stratocumulus clouds with cloud top temperatures (CTT) > −5 °C in the cold sector of extratropical cyclones over the Southern Ocean (SO) during ten SO Clouds, Radiation, Aerosol Transport Experimental Study (SOCRATES) research flights. Case studies are presented showing ice signatures within clouds when CTT were between −2 and −5°C, evidenced in Doppler radar radial velocity changes observed during high-altitude flight legs as ice particles melted across the 0°C isotherm. Ice on these legs was found to contribute to precipitation 3.8% of the time from clouds with −5°C < CTT <0°C. Clouds observed with a distinct melting level on high-altitude flight legs overall had greater cloud depths, tops with higher reflectivities, and higher linear depolarization ratios, compared to clouds without a melting level. In situ flight legs were also analyzed when Himawari-8 CTT were between 0 and −5°C and the aircraft was sampling in cloud within that temperature range. It was found that 3% of clouds sampled in situ with −5°C < CTT <0°C were mixed phase with a mean number concentration of 2.35 L^{-1} for nonspherical particles with maximum diameters >100 μm and 1.13 L^{-1} for nonspherical particles with maximum diameters >200 μm.

Plain Language Summary Pure liquid water droplets do not freeze at temperatures between 0 and −40°C, but rather become supercooled. A microscopic aerosol particle called an ice nucleating particle (INP) is required for the conversion of supercooled liquid water droplets to ice crystals. The remoteness of the Southern Ocean (SO) from continental sources of aerosol results in a paucity of particles capable of triggering ice formation in clouds. As a result, SO clouds are dominated by supercooled liquid water. Because of the small number of INPs present over the SO, and the low activity of these particles at modest supercooling, clouds with higher (>−5°C) cloud top temperatures (CTT) over the SO are not expected to produce many ice particles. Evidence provided herein shows that ice production does occur in SO clouds with CTT > −5°C. The source of INPs triggering ice nucleation is unknown, but is likely oceanic, given the remoteness of these clouds from land sources and the shallow nature of these clouds.

Key Points:

- Ice occurrence in Southern Ocean (SO) clouds was documented using remote sensing and in situ data when cloud top temperatures (CTT) were warmer than −5°C
- 3% of clouds sampled in situ with −5°C<CTT<0°C were mixed phase
- Secondary ice production processes are likely critically important for controlling ice crystal concentrations in SO clouds at warm CTT (>−5°C)

Correspondence to:
T. J. Zaremba,
tzaremb2@illinois.edu

Citation:
Zaremba, T. J., Rauber, R. M., McFarquhar, G. M., DeMott, P. J., D'Alessandro, J. J., & Wu, W. (2021). Ice in Southern Ocean clouds with cloud top temperatures exceeding −5°C. *Journal of Geophysical Research: Atmospheres*, *126*, e2021JD034574. https://doi.org/10.1029/2021JD034574

Received 11 JAN 2021
Accepted 24 JUN 2021

1. Introduction

Climatologies over the Southern Ocean (SO) reveal that more than 80% of the SO is covered by low-level clouds at any given time (e.g., Hu et al., 2010). These clouds are primarily widespread and broken stratocumulus that persist in the cold sectors of extratropical cyclones (Mace et al., 2009). The need to better simulate cloud-radiative processes and constrain the radiative heat budget in cold sectors over the SO, together with the scarcity of in situ measurements of aerosols, clouds, and precipitation to develop constraints, has motivated several recent field campaigns to better understand microphysical processes within cold-sector clouds (McFarquhar et al., 2021). During one campaign, the 2018 SO Clouds, Radiation, Aerosol Transport Experimental Study (SOCRATES), the National Science Foundation (NSF)/National Center for Atmospheric Research (NCAR) G-V aircraft conducted 15 flights from Hobart, Australia, to within ~650 km of the Antarctic coast to sample clouds, aerosols, and precipitation.

Three related characteristics of the SO cloud environment make it unique and motivated SOCRATES: the apparent paucity of ice nucleating particles (INPs) (Bigg, 1973; McCluskey et al., 2018; Welti et al., 2020)

due to it being far removed from any continental aerosol sources; the common presence of supercooled clouds, particularly in SO cyclones' cold sectors (Choi et al., 2010; Hu et al., 2010; Morrison et al., 2011); and the persistent presence of high winds over a biologically productive ocean, which can influence cloud droplet concentrations and potentially promote greater emissions of marine biogenic INPs (McCluskey et al., 2019).

The concentration of INPs active at temperatures > −5°C is limited (Kanji et al., 2017), such that INP concentrations present over oceanic regions at these temperatures lie at or below the limits of detection by current methods. For example, based on a compilation of ship campaign data, Welti et al. (2020) found that INP capable of causing immersion freezing were detected only 5% of the time when temperatures were between −5 and −7°C, meaning that 95% of the time, INP concentrations in this temperature range were below the detection limit of the measurement systems, estimated at 0.1 m^{-3}. This is consistent with observationally based parameterizations of INP concentrations from sea spray aerosol emissions in the MBL or long range transport of soil/dust INPs (McCluskey et al., 2019; Vergara-Temprado et al., 2018). Dust INPs are predicted to dominate INPs in the above-boundary layer region of the SO (McCluskey et al., 2019), where their concentration at a temperature of −5°C would be ∼0.001 m^{-3} when parameterized on the basis of regional feldspar content (Vergara-Temprado et al., 2018) or ∼0.005 m^{-3} on the basis of applying a generalized mineral dust INP parameterization (DeMott et al., 2015), which is linked to G-V measured aerosol concentrations > 0.5 μm of typically 4×10^4 m^{-3} in the above cloud region during SOCRATES. Similar INP concentrations from a direct source of sea spray aerosol emissions are also predicted. INP concentrations of 0.002 m^{-3} at −5°C are predicted by an active site density parameterization of generalized marine organic INPs when using typical marine aerosol surface areas for the SO region (McCluskey et al., 2019), and no more than 0.1 m^{-3} are predicted for any instances that might characterize enhanced organic aerosol emissions of INPs from marine organisms and their exudates (Vergara-Temprado et al., 2017). While the rare occurrence of the presence of more active terrestrially sourced dust (Harrison et al., 2016; Peckhaus et al., 2016) or microbial INPs (Pandey et al., 2016) could be postulated, the presence of such INPs is not supported by any INP observations in the SO region thus far.

The SO is a natural laboratory to study ice production processes in marine clouds largely unaffected by anthropogenic and continental aerosols. One uncertainty is how often primary and secondary ice production processes occur in these shallow clouds and if ice production is sufficient to impact cloud radiative properties. The mechanisms of ice formation in stratiform and cumuliform mixed phase clouds at temperatures greater than −10°C are not well understood (Field et al., 2017; Kanji et al., 2017) leading to uncertainty in numerical models (Khain et al., 2015; Korolev et al., 2017). Global climate models have difficulties simulating aerosol concentrations and cloud phase over the SO leading to potential inaccurate cloud-climate feedbacks (e.g., McFarquhar et al., 2021; Tan et al., 2016; Trenberth & Fasullo, 2010). Ice presence has been noted in several cumuliform (Cooper, 1986; Hobbs & Rangno, 1998; Koenig, 1963; Ladino et al., 2017; Lawson et al., 2015; Yang et al., 2020) and stratiform clouds at temperatures > −12°C (Rangno & Hobbs, 2001). Discrepancies between INP measurements and ice particle concentrations within clouds at temperatures > −10°C are attributed to secondary ice production processes (see review by Field et al., 2017).

The present study documents and quantifies the occurrence of ice in SO cold-sector clouds with cloud top temperatures (CTT) > −5°C using remote sensing and in situ data collected during SOCRATES flights. Specifically, ice presence in low-level stratocumulus cloud decks with CTT > −5°C is detected remotely through melting signatures across the 0°C isotherm in Doppler radial velocity data, and in situ by detecting nonspherical particles in optical array probe data. Case studies are presented, and a statistical summary of the occurrence of ice within these clouds is developed from the SOCRATES flights.

2. Data and Methodology

Data used in this study were collected during 15 research flights consisting of high-altitude (∼5.5 km above mean sea level (MSL)) flight legs of the NSF/NCAR G-V aircraft from Hobart, Tasmania to ∼60ºS and in situ (<3 km MSL) flight legs of the G-V from 60°S to Hobart. During the high-altitude flights the High Spectral Resolution Lidar (HSRL, Eloranta, 2005; Schwartz et al., 2019) and the High-performance Instrumented Platform for Environmental Research (HIAPER) Cloud Radar (HCR, Vivekanandan et al., 2015),

a Doppler radar, were pointed at nadir to document the structure of clouds located beneath the G-V. The HCR measured the equivalent radar reflectivity factor (Z_e) and radial velocity (V_r) below the aircraft. The algorithm presented by Ellis et al. (2019) was used to correct slight errors in the beam pointing angle away from nadir for the HCR. The method assumes that the surface echo is stationary and any offset from 0 m s^{-1} can be added or subtracted throughout the entirety of the beam using a surface V_r of 0 m s^{-1} as a reference for correction. They found that after correction the variance in V_r for the SOCRATES data set ranged from 0.24 to 0.26 m^2 s^{-2}.

The procedure for processing the HSRL and HCR data and determining the altitude, phase, and temperature of cloud top along high-altitude flight legs is presented in Zaremba et al. (2020). In brief, the HCR and HSRL were interpolated to a uniform georeferenced grid of 2-Hz temporal and 19.2 m vertical resolution. The merged HCR/HSRL data set consisted of vertical atmospheric columns that had along-track horizontal resolution of 75–110 m, depending on aircraft ground speed. Each column contained volume elements with 19.2 m vertical resolution. With the G-V flying at 5.5 km, a vertical column contained 286 volume elements, hereafter referred to as *elements*.

A curtain of dropsondes was also deployed during high-altitude flight legs to determine the thermodynamic environment present beneath the G-V (Zaremba et al., 2020). Dropsonde data were interpolated back to the closest great circle distance between the dropsonde position and the flight track (i.e., to the closest HCR/HSRL column). The dropsonde data were then interpolated using a linear interpolation over the entire high-altitude cross section to the center of all elements in the HCR/HSRL merged data set. The average dropsonde horizontal displacement between the position of the G-V and the surface was 8.4 km and the accuracy of the dropsonde temperature measurements was ±0.2°C (UCAR, 2020).

Cloud top was identified by masking clear air and aerosol signatures in the lidar data (Zaremba et al., 2020). The first unmasked element below the aircraft in each column was considered cloud top and its CTT was recorded. During the 12 high-altitude flight legs (where dropsonde measurements were made), 153,478 columns were sampled, 103,702 containing cloud top beneath the aircraft, and 39,691 with $-5°C < CTT < 0°C$.

2.1. Melting Level Identification

Ice crystals typically fall at a rate near 1 m s^{-1} whereas raindrops typically fall at a rate near 4 m s^{-1} (Pruppacher & Klett, 1997). To identify whether ice particles contributed to precipitation across the 0°C isotherm in individual columns along high-altitude flight legs with $-5°C < CTT < 0°C$, each column that had an HCR detectable signal above the noise level (Normalized Coherent Power > 0.1 or Signal to Noise Ratio > −10 dB, see Zaremba et al. (2020)), extending from cloud top downward through the 0°C isotherm was identified. A decrease in V_r from ∼−1 m s^{-1} to ∼−4 m s^{-1} detected just below the 0°C isotherm within that column implied that melting ice particles were present. No abrupt change in V_r implied that no/or a limited number of ice particles were present. To detect a melting level quantitatively, columns with $-5°C < CTT < 0°C$ were examined to determine if a decrease in radial velocity of at least 1 m s^{-1} occurred in the column over a 10 element layer (192 m). If the decrease was detected, the altitude of the top of the layer exhibiting the largest decrease in V_r was flagged as the top of a potential melting level. The potential melting level was then compared to adjacent columns. If there was less than a three element (57.6 m) difference in the altitude where the maximum decrease (>1 m s^{-1}) in V_r occurred, the level in the previous column was recorded as the melting level. This procedure was continued column by column until the melting level was no longer detected. During SOCRATES, the melting level, when present, was normally found to be ∼150–200 m below the 0°C isotherm. Melting levels were detected within 5.8% of columns during high-altitude flight legs using a 1 m s^{-1} threshold. Increasing the threshold to 1.2 m s^{-1} caused this to decrease to 5.6% of total flight leg time and decreasing the threshold to 0.8 m s^{-1} caused it to increase to 5.9%. A threshold of 1 m s^{-1} is conservative (potentially missing some melting levels) but provided detection with higher confidence. This approach identifies periods along high-altitude flight legs where ice particles are large enough and/or in high enough quantities that they form rain with fall velocities >4 m s^{-1}. Small ice particles may form drizzle after they pass through the melting level and have fall velocities <4 m s^{-1}. For this reason, the ice detection method herein should be considered a minimum bound on the frequency of ice occurrence.

2.2. Himawari-8

Himawari-8 cloud top temperatures (CTT_H) and cloud top height (CTH_H) were retrieved by the NASA SatCORPs group (Smith & Minnis, 2018) and were available at 2 km resolution every 10 min during SOCRATES flights. The NASA algorithm (Minnis et al., 2011) calculates CTT_H using the 11 μm brightness temperature. From this CTH_H is estimated using a fixed lapse rate assumption where the surface temperature was estimated using a running 24-h mean surface air temperature from numerical weather reanalysis and a fixed lapse rate of −7.1 K km^{-1} (Minnis et al., 2011). Brightness temperature is determined from radiation emitted over a depth of the cloud top layer that depends on the cloud's emissivity. Under most conditions brightness temperature typically has an uncertainty of 1 K. An inaccurate sea surface temperature estimate and/or lapse rate different from −7.1 K km^{-1} could result in CTH_H errors, although these are smaller for shallow clouds.

Himawari-8 CTT_H and CTH_H were used to obtain an overall perspective of the environment that the G-V was sampling over the SO during individual high-altitude flight legs and was used to estimate CTT and CTH during in situ flight legs. Dropsonde estimated CTT and lidar detected CTH were averaged every 10 s (or less for broken clouds) along the G-V's flight track in order to compare the nearest neighbor Himawari-8 satellite pixel to CTT and CTH observed by the G-V along high-altitude flight legs.

Furthermore, to ensure that ice particles were not arriving from undetected, deeper clouds along the mean wind direction upstream of the flight track, and seeding lower clouds, probability density functions of Himawari-8 CTT_H were developed for all clouds within a distance (D) upstream of the flight track when melting was detected. D was calculated from $D = ud / V_{r,s}$ where u is the maximum wind speed in the −10°C to 0°C layer, $V_{r,s}$ is the fall speed of ice particles, estimated from V_r as 1.0 m s^{-1}, and d is fall distance between the altitudes of the −10 and 0°C isotherm. The −10°C level was chosen based on (Zaremba et al., 2020, their Figure 19) which showed that 85% of all cloud tops measured by the G-V had CTT > −10°C. SOCRATES flights focused on the cold sectors of extratropical cyclones where typical clouds are broken stratocumulus or solid stratocumulus cloud decks. Most clouds in the Zaremba et al. (2020) study with CTT < −10°C were sampled in closer proximity to frontal clouds of extratropical cyclones (e.g., Rauber et al., 2020). None of the cases presented here fell into this category. The value of D ranged from 20.8 km in light wind conditions to 102.6 km when strong winds were present. Himawari-8 data closest in time to the detection of a melting level by the aircraft was used to calculate probability density functions over the distance D from the aircraft flight track.

2.3. Optical Array Probe and Cloud Liquid Water Measurements

In situ flight legs were conducted during SOCRATES while the G-V was returning to Hobart (McFarquhar et al., 2021). During these legs the aircraft flew up to four flight patterns at altitudes <3 km. The first was straight, level flight just above boundary-layer cloud top (~2–3 km MSL). The second was straight, level flight just above the ocean surface beneath cloud base. The third were sawtooth patterns up and down through cloud. On some occasions, the G-V also flew level legs near cloud top, after the level leg above cloud, when conditions were deemed safe to avoid aircraft icing. During sawtooth flight legs the HCR and HSRL were typically pointed at nadir on descent and zenith on ascent. This limited the amount of data available to assess cloud phase and ice particle concentrations in the temperature range 0 to −5°C. The only simultaneous measurement of CTT while the aircraft was sampling between 0 and −5°C was from the Himawari-8. The analysis herein therefore is restricted to periods when CTT_H were between 0 and −5°C and the G-V was sampling between 0 and −5°C. In situ flight leg times used in this analysis to identify periods where CTT_H were between 0 and −5°C are summarized in Table 1.

The machine learning algorithm of D'Alessandro et al. (2021) was used to estimate cloud phase based on simulations acquired by several cloud physics probes during in situ legs. Measurements from a 2D Stereo Probe (2D-S) were used to estimate the concentrations of liquid and/or ice phase hydrometeors. 2D-S data in this analysis was processed using the University of Illinois/Oklahoma OAP Processing Software (McFarquhar et al., 2018; Wu & McFarquhar, 2019). The 2D-S nominally measures particles with a resolution of 10 μm between 10 μm < D < 3,200 μm, but measurements for particles with maximum dimensions (D_{max}) less than 100–150 μm are highly uncertain due to a small and poorly defined depth of field for small particles (see McFarquhar et al., 2017 and references therein). The D_{max} of ice particles was calculated using the algorithm of Wu and McFarquhar (2016). Ice particle shape was determined using the algorithm of

Table 1
In Situ Flight Leg Start/End Times

Research Flight	Start time	End time	GV track length
RF01	2018-01-16 01:52:00 UTC	2018-01-16 02:48:00 UTC	54 km
RF02	2018-01-19 03:34:00 UTC	2018-01-19 06:34:00 UTC	1,265 km
RF03	2018-01-22 23:51:00 UTC	2018-01-23 03:18:00 UTC	969 km
RF04	2018-01-24 02:11:00 UTC	2018-01-24 04:06:00 UTC	701 km
RF05	2018-01-26 00:55:00 UTC	2018-01-26 05:04:00 UTC	1,002 km
RF06	2018-01-29 01:30:00 UTC	2018-01-29 03:31:00 UTC	733 km
RF07	2018-01-31 03:29:00 UTC	2018-01-31 07:15:00 UTC	996 km
RF08	2018-02-04 02:04:00 UTC	2018-02-04 05:45:00 UTC	1,046 km
RF09	2018-02-05 02:43:00 UTC	2018-02-05 05:03:00 UTC	933 km
RF10	2018-02-08 00:05:00 UTC	2018-02-08 04:04:00 UTC	1,635 km
RF11	2018-02-17 03:22:00 UTC	2018-02-17 04:57:00 UTC	254 km
RF12	2018-02-18 02:55:00 UTC	2018-02-18 05:19:00 UTC	246 km
RF13	2018-02-20 01:54:00 UTC	2018-02-20 06:28:00 UTC	1,708 km
RF14	2018-02-22 01:56:00 UTC	2018-02-22 04:58:00 UTC	976 km
RF15	2018-02-24 04:18:00 UTC	2018-02-24 08:33:00 UTC	1,063 km

Holroyd (1987), which identifies particles as spherical or one of a number of nonspherical shapes. In this paper we report concentrations of nonspherical particles with $D_{max} > 100$ and >200 μm.

2.4. CTT Uncertainties

CTT during the remote sensing flight legs was determined from lidar-detected cloud top heights in each column and dropsonde measurements of temperature along the flight track linearly interpolated to each column. Dropsonde spacing ranged from 89.5 to 307.8 km, with an average spacing of 189 km (see Zaremba et al., 2020; their Table 1). Uncertainty in CTT estimates will arise where temperature changes nonlinearly between dropsondes at altitudes corresponding to the cloud tops between dropsondes. Unfortunately, it was not possible to assess this uncertainty quantitatively because measurements of temperature at a frequency greater than the dropsonde measurements were not available. Cross sectional plots of temperature along the entire flight track from European Centre for Medium-Range Weather Forecasts ERA5 reanalysis were examined to determine if nonlinear variations in temperature were obvious between positions of dropsonde launches in regions where melting layers were detected (none were), largely because the measurements reported herein were all within the cold sector of SO cyclones, well distanced from frontal boundaries. Nevertheless, this uncertainty in CTT is present, and the results should be interpreted with this uncertainty in mind.

Uncertainty is also present in estimates of Himawari-8 CTT both because of the uncertainty in the retrieval based on radiance measurements, and because the satellite estimates CTT and CTH are based on averages over an approximate 2 × 2 km area, which is a much larger area than the lidar or in situ measurements.

3. Case Studies of Ice Presence at Warm CTT

Of the 12 high-altitude flight legs, 11 had periods with clouds with 0°C > CTT ≥ −5°C. Of these, eight flights had segments where ice was present at CTT ≥ −5°C along some portion of the flight track. During four of these flights, Himawari-8 CTT_H upstream within D had at least one grid pixel with $CTT_H < -7$°C. The remaining four flights had segments where ice presence occurred at CTT ≥ −5°C and CTT_H upstream within D were all ≥ −7°C, with nearly all Himawari-8 grid pixels having $CTT_H \geq -5$°C. It can therefore be inferred that ice production by primary and secondary ice production processes occurred in these cases at CTT ≥ −5°C. Examples of two flight segments are presented below, followed by a statistical summary of high-altitude flight legs in Section 4.

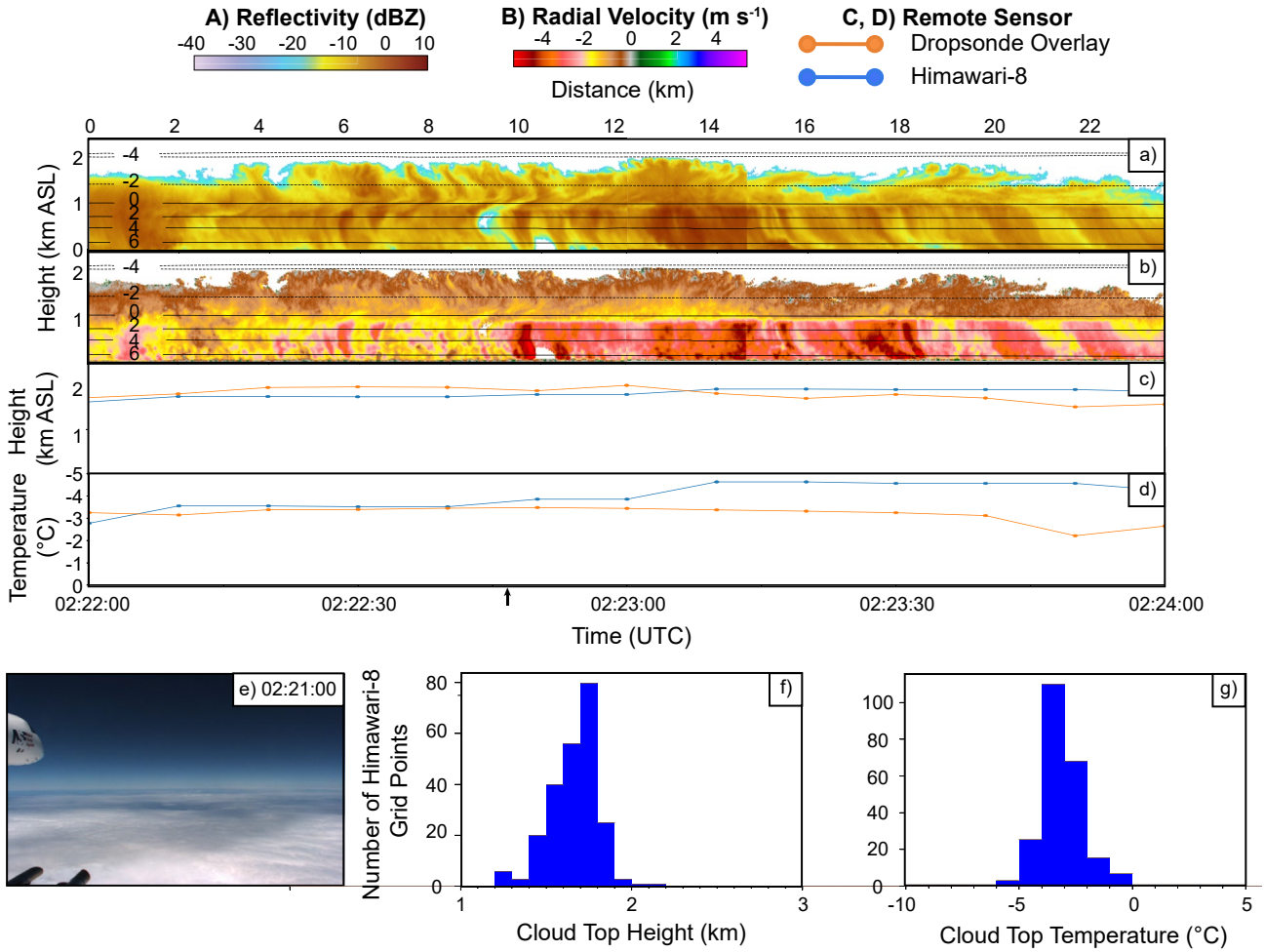

Figure 1. RF02 10-Hz HCR (a) Z_e and (b) V_r data from January 19, 2018 02:22:00 and 02:24:00 UTC. Temperature (°C) is overlaid; (c) cloud top temperatures (CTT) and (d) cloud top height (CTH) detected by the G-V (red) and Himawari-8 (blue). The arrow marks 02:22:48 UTC. (e) Flight level forward camera imagery at 02:21:00; (f and g) Distribution of Himawari-8 CTH and CTT within D upstream of the flight track.

3.1. Research Flight 02: January 19, 2018 02:22:00-02:22:24 UTC

Figure 1 shows an example of Z_e and V_r from passage over a stratocumulus cloud deck with $-5°C < CTT < -3°C$ based on temperatures measured by both the dropsondes and Himawari-8 temperature retrievals along the flight track. No clouds were detected by the lidar above the stratocumulus deck between the aircraft and ~2 km. Between January 19, 2018 02:22:00 and 02:22:48 UTC, distinct radar signatures of melting ice were not evident. Beginning at 02:22:48 UTC, a distinct signature of melting is evident in the V_r field. At this location, Himawari-8 CTT_H along the flight track were ~2°C less than dropsonde estimated CTT, but both were >−5°C. Flight-level forward camera images confirmed the absence of higher cloud layers that could be a source of ice particles (Figure 1e). A region 0–82.5 km upstream (west) of the melting level was checked using Himawari-8 data to determine if clouds upstream could have seeded the clouds where ice was observed. Clouds upstream had CTT that were all > −6°C and CTH that were all <2.1 km (Figure 1f and 1g). In this case, seeding by upstream higher clouds was not evident, and it can be inferred that ice production occurred within the clouds at CTT > −5°C.

3.2. Research Flight 14: February 22, 2018 01:22:00–01:24:00 UTC

Figure 2 shows an example of ice presence within stratocumulus clouds with $-5°C < CTT < -3°C$ during RF14. Ice presence was evident in the V_r field beneath cloud top between February 22 01:22:23 UTC

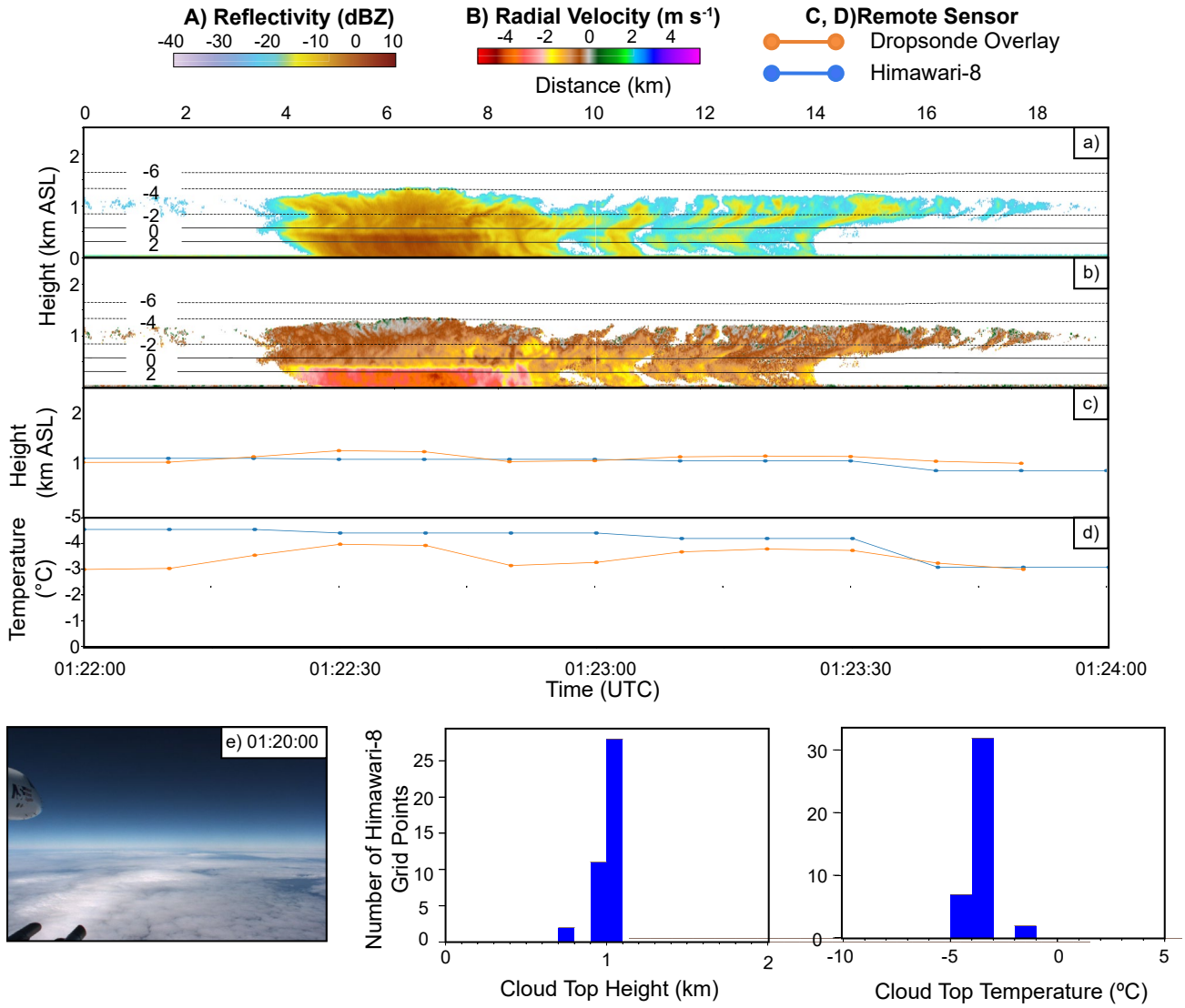

Figure 2. Same as Figure 1 but for RF14 from February 22, 2018 01:29:00 and 01:32:00 UTC. Flight level imagery (e) is shown from 01:20:00 UTC.

and 01:22:53. CTT > −5°C were confirmed by both Himawari-8 measurements and dropsonde estimates. The G-V and Himawari-8 measured CTT > −5°C beginning at 01:22:00. Himawari-8 measured CTT were ~1.5°C lower than the G-V observed cloud tops, but both were > −5°C. Beyond 01:23:30 the Himawari-8 and G-V measured CTT were approximately equivalent, again > −5°C. Flight level forward camera images (Figure 2e) confirm the absence of higher cloud layers. A region 0–69.4 km west of the melting level was checked using Himawari-8 data to determine if clouds with lower CTT were present upstream. Clouds upstream had CTT that were all > −4.4°C and CTHs that were all <1.1 km (Figure 2f and 2g). In this case, seeding by higher clouds again was not evident.

4. Statistics on Ice Presence at Warm CTT Along High-Altitude Flight Legs

Ice presence at CTT ≥ −5°C during SOCRATES high-altitude flight legs was quantified based on the number of columns sampled by the G-V. There were 39,691 columns where CTT sampled by the HSRL along the flight track were in the range (−5°C < CTT < 0°C). On Figure 3 the blue bars show the distribution of these columns as a function of CTT. Of these 39,691 columns, 36.2% had an HCR detectable signal above

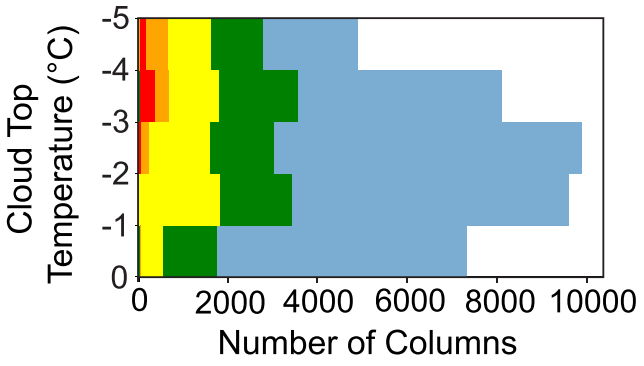

Figure 3. Number of columns where cloud top was detected using the High Spectral Resolution Lidar (HSRL) and cloud top temperatures (CTT) were between 0 and −5°C (blue), the subset of columns with an HIAPER Cloud Radar (HCR) detectable signal above the noise level extending beneath cloud top (green), the subset of columns that met the above criteria and had an HCR detectable signal above the noise level extending beneath the 0°C isotherm (yellow), subset of columns that met the above criteria and also satisfied the V_r criteria for the existence of a melting level (orange), subset of columns that met the above criteria and had CTT upstream within D that were all >−7°C (red).

the noise level extending beneath cloud top, also shown on Figure 3 as a function of CTT (green bars – 14,468 columns). 18.2% met the above criteria and had an HCR detectable signal above the noise level extending beneath the 0 °C isotherm (yellow – 7,224 columns). 3.8% met the above criteria and also satisfied the V_r criteria for the existence of a melting level (orange –1,508 columns). 1.3% met the above criteria and had CTT_H upstream within D that were all > −7°C (red –516 columns). Figure 3 also shows that ice was only present when CTT were <−2°C. Although the presence of radar detectable ice when CTT were >−5°C was infrequent, implying that the warm rain process/supercooled warm rain process play a dominant role in low-level cold sector SO clouds, the ice phase and ice production at CTT > −5°C does occur and impacts precipitation and cloud structure.

5. Comparison of Cloud Characteristics

Cloud top and cloud depth characteristics sampled remotely during high-altitude flight legs were further analyzed using HSRL and HCR data to compare characteristics when melting levels were present and absent. When CTT were between 0 and −5°C and a melting level was detected, the cloud top mean and standard deviation of Z_e was −0.3 ± 8.7 dBZ_e, while it was −8.3 ± 9.6 dBZ_e when a melting level was absent (Figure 4a). This suggests that larger and/or more particles were present at cloud top when melting levels were detected. These likely were ice particles instead of cloud drops, although large drizzle drops can produce higher values of Z_e.

The cloud top V_r was −0.7 ± −0.5 m s^{-1} when a melting level was detected and −0.9 ± 0.6 m s^{-1} when a melting level was not present (Figure 4b). Clouds without a melting level had a wider range of V_r at cloud top with a tail in V_r approaching −4 m s^{-1}, characteristic of the presence of drizzle. V_r was typically slightly more negative at cloud top when a melting level was detected, consistent with the difference in fall velocities between ice particles and cloud droplets. However, in some clouds with no melting level detected, drizzle and raindrops were likely present, contributing to the negative tail in the distribution of V_r.

HSRL backscatter coefficients when melting levels were, and were not detected were −5.3 ± 2.1 m^{-1} sr^{-1} and −5.5 ± 2.1 m^{-1} sr^{-1}, respectively, essentially exhibiting no difference. Particle linear depolarization ratios (δ_p) at cloud top when a melting level was present were 0.13 ± 0.13, compared to 0.17 ± 0.07 when no melting level was present (Figure 4d). The shift to higher values is consistent with differences between ice and water. However, the distribution of δ_p had a secondary mode in δ_p when no melting level was present (Figure 4d). These elements typically occurred at the topmost cloud top element. It is unclear what the source of the second mode was in these cases.

Cloud depth was defined as the distance between the topmost cloud top element and the element at the lowest altitude where either an HSRL cloud was detected or HCR reflectivity was above the noise level. Clouds where a melting layer was detected had a depth of 1.5 ± 0.5 km compared to 0.8 ± 0.7 km when no melting layer was detected (Figure 4e). These results indicate that deeper clouds tended to produce ice, even though their top temperatures were ≥−5°C.

6. In Situ Statistics on Ice Presence at Warm CTT

D'Alessandro et al.'s (2021, their Figure 4) analysis of in situ SOCRATES data showed ice or mixed phase conditions occurring ∼20% of the time at temperatures between −5 and 0°C, although the CTT was not considered in their analyses. In the analysis below we now consider CTT. Ice presence at CTT > −5°C during SOCRATES in situ flight legs was quantified based on the number of 1 Hz in situ samples made by the G-V based on the machine learning algorithm of D'Alessandro et al. (2021). Time periods were isolated when CTT_H were between 0 and −5°C and the G-V was sampling in that temperature range. Only 4.3% of

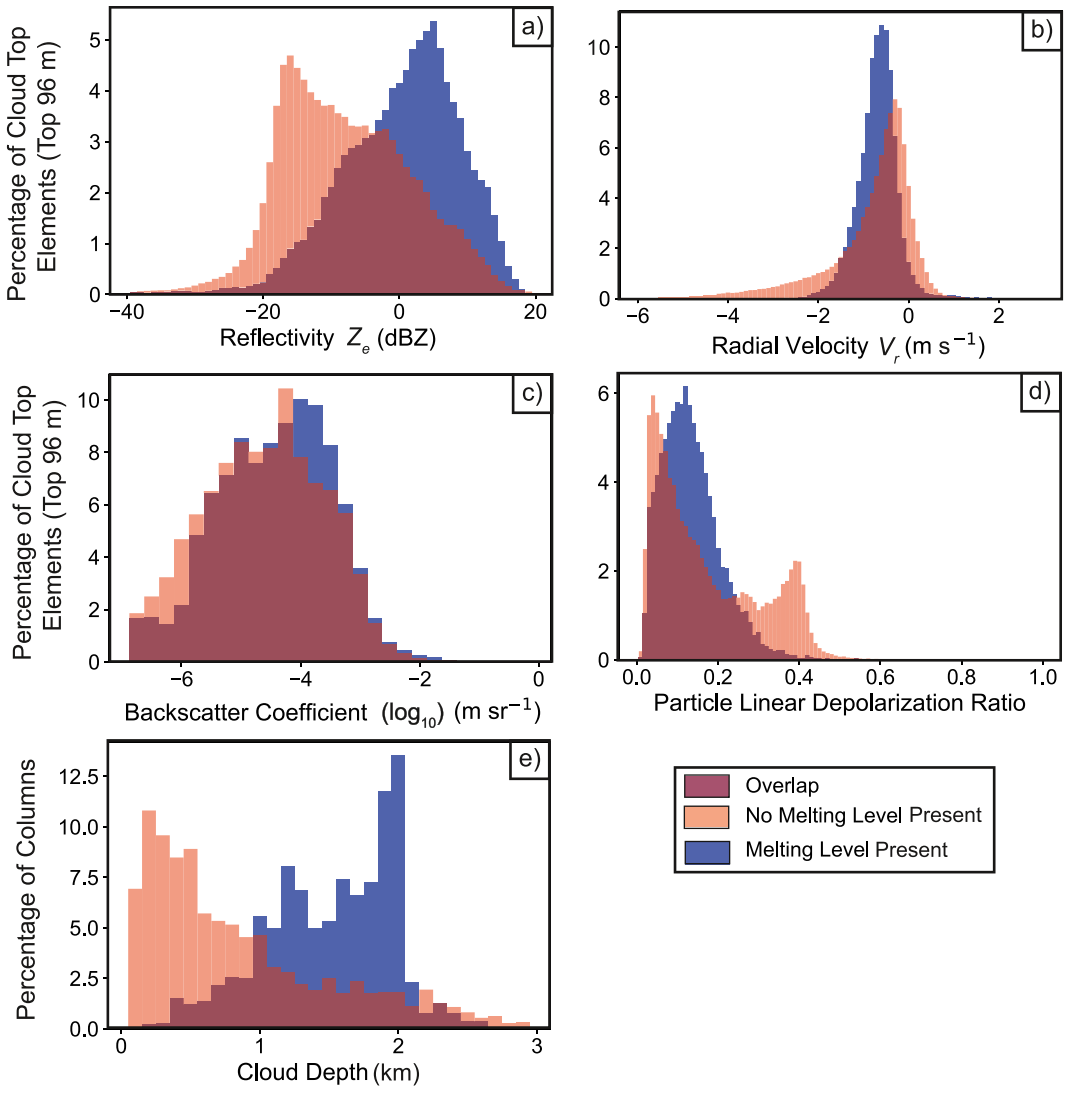

Figure 4. Cloud top characteristics and cloud depth for columns where a melting level was present (blue) and not present (pink) during Southern Ocean Clouds, Radiation, Aerosol Transport Experimental Study (SOCRATES) high altitude flight legs. Percentage of elements within 96 m of cloud top for (a) Z_e binned every 1 dBZ, (b) V_r binned every 0.1 m s^{-1}, (c) backscatter coefficient binned every 0.25 m sr^{-1}, and (d) particle linear depolarization ratio binned every 0.01. (e) is the percentage of columns with a given cloud depth, as defined in the text binned every 0.1 km.

the total in situ flight leg time during SOCRATES met these criteria. Figure 5a shows a summary of 1 Hz temperatures sampled when these conditions were met. Figure 5b and 5c shows a summary of cloud phase determined using D'Alessandro et al. (2021). Out of all the time periods where CTT_H were between 0 and −5°C, 97% of the 1 Hz in situ samples were liquid phase and 3% were mixed phase, meaning nonspherical particles were present in a given 1 Hz sample (Figure 5b). Mixed phase conditions when CTT_H were >−5°C were found on eight research flights (Figure 5c). Most flights had very limited sampling time (<30 s) where ice was present and CTT were between 0 and −5°C. During 1 Hz mixed phase periods, 2D-S number concentrations for nonspherical particles with $D_m > 100$, and $D_m > 200$ μm were analyzed. During 1 Hz mixed phase periods the average number concentration for nonspherical particles with $D_{max} > 100$ μm were 2.35 L^{-1} and $D_{max} > 200$ μm were 1.13 L^{-1} (Figure 5d). The average number concentration for spherical particles during 1 Hz mixed phase periods with $D_{max} > 100$ μm were 0.09 L^{-1}, and $D_{max} > 200$ μm were 0.01 L^{-1} (Figure 5e). This implies that particles sampled with $D_{max} > 100$ μm were essentially all nonspherical and presumably ice.

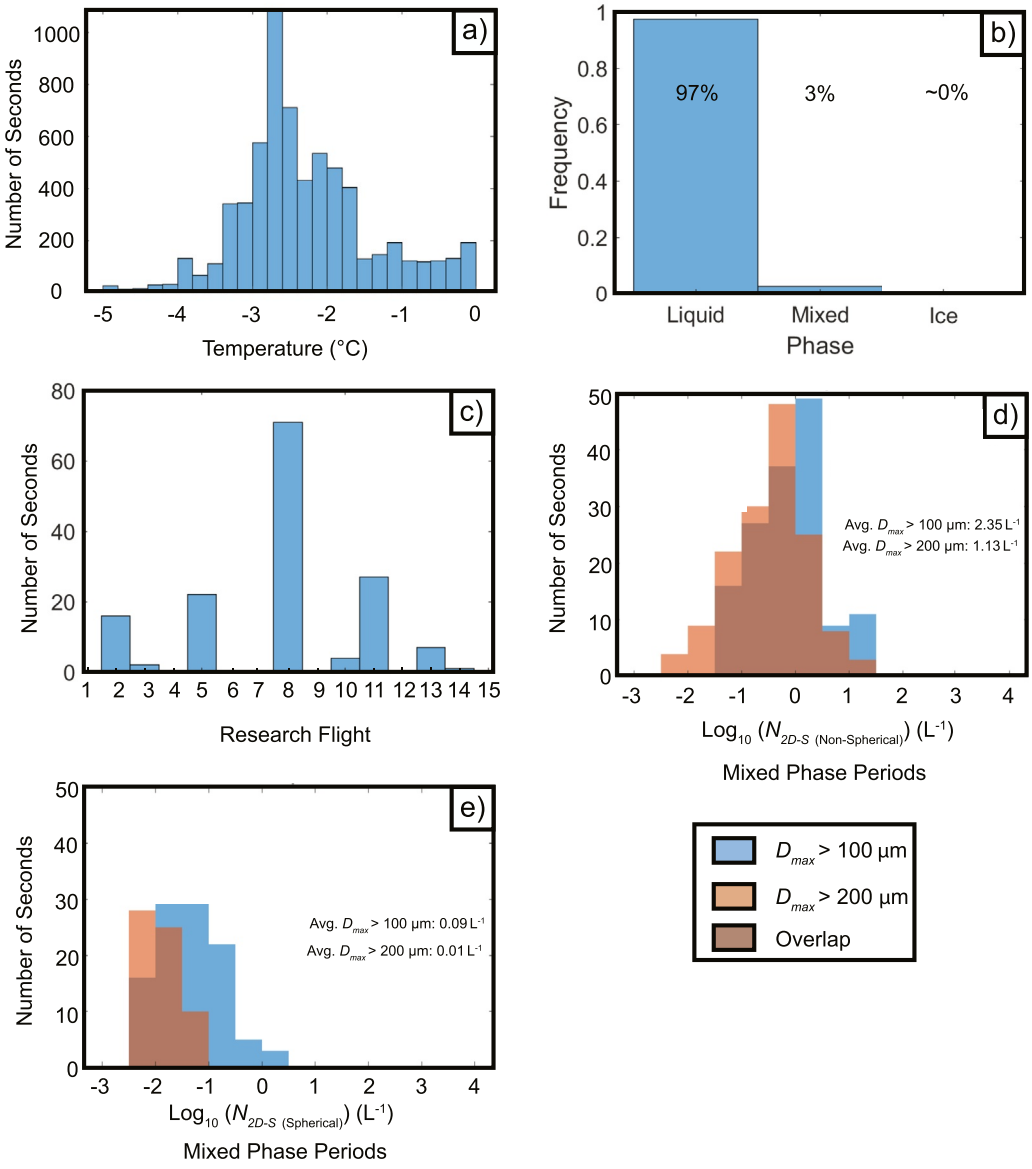

Figure 5. (a) number of in-cloud 1 Hz samples at $0 > T > -5$°C when CTT_H were between 0 and −5°C. (b) cloud phase determined using the D'Alessandro et al. (2021) algorithm for these samples. (c) number of seconds where mixed phase cloud was detected on each research flight for these samples. (d) particle concentrations ($N_{2D\text{-}S}$) of nonspherical particles with $D_m > 100$ µm and $D_m > 200$ µm when mixed phase 1 Hz samples were detected. (e) particle concentrations ($N_{2D\text{-}S}$) of spherical particles with $D_m > 100$ µm and $D_m > 200$ µm during 1 Hz mixed phase samples.

Note that spherical particles with $D_{max} < 100$ µm could have been ice particles. There was not enough information to determine this explicitly using the 2D-S because very few pixels were shadowed. This made it difficult to differentiate between spherical and nonspherical particles and therefore differentiate between liquid and ice for particles with $D_{max} < 100$ µm. The sampling volume of the 2D-S was 8 L s^{-1} which limited the total volume sampled when $0 > CTT_H > -5$°C. For these reasons, the reported concentrations for nonspherical particles should be regarded as a minimum concentration for ice particles.

7. Summary and Conclusions

The nonspherical particle number concentration average for $D_{max} > 200$ μm was 1.13 L^{-1} for mixed phase 1 Hz samples. The ability of clouds to produce ice at CTT > −5°C at these concentrations over the SO is unexpected because of the low INP concentrations active at such temperatures. The observed ice particle concentrations were 3–4 orders of magnitude greater than INP concentrations measured by the G-V during SOCRATES at −12°C (0.001–0.01 L^{-1}), the highest temperature of detection (see data availability). These ice concentrations imply that secondary ice production processes must be active in ∼3%–4% of SO clouds with CTT > −5°C, as independently shown in both the remote sensing and in situ analyses.

The complicated nature and limited understanding of ice production at high CTT has made it difficult to pinpoint the source of INPs or the physical mechanisms behind primary and secondary ice formation within these modestly supercooled low-level clouds. It is certain that secondary ice production processes (e.g., Field et al., 2017) contributed to glaciation of the clouds, contributing to the observed remote sensing signal, but for secondary ice particle formation to activate, primary ice nucleation must have first occurred. The source of INPs triggering ice nucleation remains unknown, but is likely oceanic, given the remoteness of the clouds from land sources and the shallow nature of the clouds. Measurements have thus far attributed INP to oceanic sources over the region (McCluskey et al., 2019).

This study demonstrated the existence of ice at CTT > −5°C within SO clouds from a remote sensing and in situ perspective.

The key findings are as follows:

1. The presence of ice was documented over the SO at CTT > −5°C during 8 of 12 high-altitude research flights from a remote sensing perspective. Cases of ice presence at high CTT were analyzed using Himawari-8 data to determine if clouds upstream were potentially seeding clouds observed by the aircraft. Four research flights had cases where ice presence at high CTT (>−5°C) showed no evidence of upstream seeding.
2. Example case studies from two research flights were presented to illustrate ice presence and inferred production evidenced by ice particles melting across the 0°C isotherm in V_r data when CTT were between −2 and −5°C. Himawari-8 CTT measurements confirmed that CTT were >−5°C over and upstream of the region observed by the G-V aircraft.
3. Of clouds sampled remotely by the G-V aircraft during SOCRATES, 38.3% had −5°C < CTT <0°C. Of these clouds, 3.8% showed evidence of ice presence, as evidenced by a distinct melting level and 1.3% had ice present with no evidence of high clouds upstream. This is likely a lower bound for ice production. This percentage is, however, consistent with the compilation of measurements from Welti et al. (2020) that showed that immersion freezing INP exceeding 0.1 m^{-3} were detected 5% of the time between −7 and −5°C.
4. Clouds that had a melting level present and CTT ≥ −5°C observed remotely on high-altitude flight legs had cloud tops (top 96 m) with higher reflectivities, higher linear depolarization ratios, and deeper cloud depths compared to cloud tops without a melting level present.
5. Of the clouds sampled in situ by the G-V during SOCRATES, 4.3% had Himwari-8 CTT between 0 and −5°C while the aircraft sampled in situ between 0 and −5°C. Of these clouds 97% were liquid phase and 3% were mixed phase. Mixed phase clouds had mean number concentrations of 2.35 L^{-1} for nonspherical particles with maximum diameters >100 μm and 1.13 L^{-1} for nonspherical particles with maximum diameters >200 μm.

Secondary ice production processes are likely critically important for controlling ice crystal concentrations found in SO clouds at warmer CTT > −5°C. One question has been how often primary and secondary ice production processes occur in these shallow clouds. The analyses presented in this paper quantify the occurrence of ice at CTT > −5°C and thereby provide a constraint on numerical modeling simulations of the microphysics of clouds in the cold sectors of extratropical cyclones over the SO, a primary goal of SOCRATES. Future work should focus on the impact of ice production on cloud radiative and precipitation processes within these modestly supercooled clouds.

Data Availability Statement

The data that support the findings of this study can be obtained at the following addresses: HCR radar time series data: https://doi.org/10.5065/D6D7998S. Dropsonde data: https://doi.org/10.5065/D6QZ28SG. HSRL data: https://doi.org/10.5065/D64J0CZS. NASA SatCORPS Himawari Cloud Retrieval Data: https://doi.org/10.5065/D6CC0ZFJ. 2D-S Data: https://doi.org/10.26023/8HMG-WQP3-XA0X. INP Data: https://data.eol.ucar.edu/dataset/552.044 and https://data.eol.ucar.edu/dataset/552.045.

Acknowledgments
This work was supported by the National Science Foundation (Grants AGS 1628674, AGS1660486, and AGS1762096). The authors appreciate the efforts of the entire SOCRATES team in collecting a high-quality data set. We also appreciate the efforts of Michael Dixon and Dr. Ulrike Romatschke in building the merged 2 Hz HCR/HSRL data set. The authors also would like to thank Dr. Scott Ellis and Dr. Jothiram Vivekanandan for answering our questions regarding the HCR and Dr. Matt Hayman for answering our questions regarding the HSRL. The authors also appreciate the efforts of Dr. William Smith and the NASA Langley Cloud and Radiation Research Group for building the Himawari-8 cloud retrieval data set used in this analysis.

References

Bigg, E. K. (1973). Ice nucleus concentrations in remote areas. *Journal of the Atmospheric Sciences*, *30*, 1153–1157. https://doi.org/10.1175/1520-0469(1973)030<1153:INCIRA>2.0.CO;2

Choi, Y. S., Ho, C. H., Kim, S. W., & Lindzen, R. S. (2010). Observational diagnosis of cloud phase in the winter Antarctic atmosphere for parameterizations in climate models. *Advances in Atmospheric Sciences*, *27*, 1233–1245. https://doi.org/10.1007/s00376-010-9175-3

Cooper, W. A. (1986). Precipitation enhancement: A scientific challenge: Ice initiation in natural clouds. *Meteorological Monographs*, *43*, 29–32. https://doi.org/10.1175/0065-9401-21.43.29

D'Alessandro, J. J., McFarquhar, G. M., Wu, W., Stith, J. L., Jensen, J. B., & Rauber, R. M. (2021). Characterizing the occurrence and spatial heterogeneity of liquid, ice, and mixed phase low-level clouds over the Southern Ocean using in situ observations acquired during SOCRATES. *Journal of Geophysical Research: Atmospheres*, e2020JD034482. https://doi.org/10.1029/2020JD034482

DeMott, P. J., Prenni, A. J., McMeeking, G. R., Sullivan, R. C., Petters, M. D., Tobo, Y., et al. (2015). Integrating laboratory and field data to quantify the immersion freezing ice nucleation activity of mineral dust particles. *Atmospheric Chemistry and Physics*, *15*(1), 393–409. https://doi.org/10.5194/acp-15-393-2015

Ellis, S. M., Tsai, P., Burghart, C., Romatschke, U., Dixon, M., Vivekanandan, J., et al. (2019). Use of the Earth's Surface as a Reference to Correct Airborne Nadir-Looking Radar Radial Velocity Measurements for Platform Motion. *Journal of Atmospheric and Oceanic Technology*, *36*, 1343–1360. https://doi.org/10.1175/JTECH-D-19-0019.1

Eloranta, E. (2005). High spectral resolution lidar. In C. Weitkamp (Ed.), *Lidar: Range-Resolved optical remote sensing of the atmosphere*. Springer series in optical sciences (pp. 143–163). Springer-Verlag. https://doi.org/10.1007/b106786

Field, P. R., Lawson, R. P., Brown, P. R., Lloyd, G., Westbrook, C., Moisseev, D., et al. (2017). Ice formation and evolution in clouds and precipitation: Measurement and modeling challenges: Secondary ice production: Current state of the science and recommendations for the future. *Meteorological Monographs*, 58, 7.1–7.20.

Harrison, A. D., Whale, T. F., Carpenter, M. A., Holden, M. A., Neve, L., O'Sullivan, D., et al. (2016). Not all feldspars are equal: A survey of ice nucleating properties across the feldspar group of minerals. *Atmospheric Chemistry and Physics*, *16*, 10927–10940. https://doi.org/10.5194/acp-16-10927-2016

Hobbs, P. V., & Rangno, A. L. (1998). Microstructures of low and middle- level clouds over the Beaufort Sea. *Quarterly Journal of the Royal Meteorological Society*, *124*(550), 2035–2071. https://doi.org/10.1002/qj.49712455012

Holroyd, E. W. (1987). Some techniques and uses of 2D-C habit classification software for snow particles. *Journal of Technology*, *4*(3), 498–511. https://doi.org/10.1175/1520-0426(1987)004<0498:STAUOC>2.0.CO;2

Hu, Y., Rodier, S., Xu, K., Sun, W., Huang, J., Lin, B., et al. (2010). Occurrence, liquid water content, and fraction of supercooled water clouds from combined CALIOP/IIR/MODIS measurements. *Journal of Geophysical Research: Atmospheres*, *115*, D00H34. https://doi.org/10.1029/2009JD012384

Kanji, Z. A., Ladino, L. A., Wex, H., Boose, Y., Burkert-Kohn, M., Cziczo, D. J., & Krämer, M. (2017), Overview of Ice Nucleating Particles. *Meteorological Monographs*, 58, 1.1–1.33. https://doi.org/10.1175/AMSMONOGRAPHS-D-16-0006.1

Khain, A. P., Beheng, K. D., Heymsfield, A., Korolev, A., Krichak, S. O., Levin, Z., et al. (2015). Representation of microphysical processes in cloud-resolving models: Spectral (bin) microphysics versus bulk parameterization. *Reviews of Geophysics*, *53*, 247–322. https://doi.org/10.1002/2014RG000468

Koenig, L. R. (1963). The glaciating behavior of small cumulonimbus clouds. *Journal of the Atmospheric Sciences*, *20*, 29–47. https://doi.org/10.1175/1520-0469(1963)020<0029:TGBOSC>2.0.CO;2

Korolev, A., McFarquhar, G. M., Field, P. R., Franklin, C., Lawson, P., Wang, Z., et al. (2017). Ice formation and evolution in clouds and precipitation: Measurement and modeling challenges: Mixed-phase clouds: Progress and challenges. *Meteorological Monographs*, 58, 5.1–5.50. https://doi.org/10.1175/AMSMONOGRAPHS-D-17-0001.1

Ladino, L. A., Korolev, A., Heckman, I., Wolde, M., Fridlind, A. M., & Ackerman, A. S. (2017). On the role of ice-nucleating aerosol in the formation of ice particles in tropical mesoscale convective systems. *Geophysical Research Letters*, *44*, 1574–1582. https://doi.org/10.1002/2016gl072455

Lawson, R. P., Woods, S., & Morrison, H. (2015). The microphysics of ice and precipitation development in tropical cumulus clouds. *Journal of the Atmospheric Sciences*, *72*, 2429–2445. https://doi.org/10.1175/jas-d-14-0274.1

Mace, G. G., Zhang, Q., Vaughan, M., Marchand, R., Stephens, G., Trepte, C., & Winker, D. (2009). A description of hydrometeor layer occurrence statistics derived from the first year of merged Cloudsat and CALIPSO data. *Journal of Geophysical Research*, *114*, D00A26. https://doi.org/10.1029/2007JD009755

McCluskey, C. S., DeMott, P. J., Ma, P. L., & Burrows, S. M. (2019). Numerical representation of marine ice-nucleating particles in remote marine environment observations. *Geophysical Research Letters*, *46*, 7838–7847. https://doi.org/10.1029/2018GL081861

McCluskey, C. S., Hill, T. C., Humphries, R. S., Rauker, A. M., Moreau, S., Strutton, P. G., et al. (2018). Observations of ice nucleating particles over Southern Ocean waters. *Geophysical Research Letters*, *45*(11), 11989–11997. https://doi.org/10.1029/2018GL079981

McFarquhar, G. M., Baumgardner, D., Bransemer, A., Abel, S. J., Crosier, J., French, J., & Um, J. (2017). Processing of ice cloud in situ data collected by bulk water, scattering, and imaging probes: Fundamentals, uncertainties, and efforts toward consistency. *Meteorological Monographs*, 58, 11.1–11.33. https://doi.org/10.1175/AMSMONOGRAPHS-D-16-0007.1

McFarquhar, G. M., Bretherton, C., Marchand, R., Protat, A., DeMott, P., Alexander, A., et al. (2021). Observations of clouds, aerosols, precipitation, and surface radiation over the Southern Ocean: An overview of CAPRICORN, MARCUS, MICRE and SOCRATES. *Bulletin of the American Meteorological Society*. Early Online Release. https://doi.org/10.1175/bams-d-20-0132.1

McFarquhar, G. M., Finlon, J. A., Stechman, D. M., Wu, W., Jackson, R. C., & Freer, M. (2018). *University of Illinois/Oklahoma optical array probe (OAP) processing software*. Retrieved from https://10.5281/ZENODO.1285969

Minnis, P., Sun-Mack, S., Young, D. F., Heck, P. W., Garber, D. P., Chen, Y., & Yang, P. (2011). CERES edition-2 cloud property retrievals using TRMM VIRS and Terra and Aqua MODIS data—Part I: Algorithms. *IEEE Transactions on Geoscience and Remote Sensing*, *49*(11), 4374–4400. https://doi.org/10.1109/TGRS.2011.2144601

Morrison, A. E., Siems, S. T., & Manton, M. J. (2011). A three-year climatology of cloud-top phase over the Southern Ocean and North Pacific. *Journal of Climate*, *24*, 2405–2418. https://doi.org/10.1175/2010jcli3842.1

Pandey, R., Usui, K., Livingstone, R. A., Fischer, S. A., Pfaendtner, J., Backus, E. H. G., et al. (2016). Ice-nucleating bacteria control the order and dynamics of interfacial water. *Scientific Advances*, *2*(4), e1501630. https://doi.org/10.1126/sciadv.1501630

Peckhaus, A., Kiselev, A., Hiron, T., Ebert, M., & Leisner, T. (2016). A comparative study of K-rich and Na/Ca-rich feldspar ice nucleating particles in a nanoliter droplet freezing assay. *Atmospheric Chemistry and Physics*, *16*, 11477–11496. https://doi.org/10.5194/acp-16-11477-2016

Pruppacher, H. R., & Klett, J. D. (1997). *Microphysics of clouds and precipitation* (Ed. 2). Springer Inc., (p. 954).

Rangno, A. L., & Hobbs, P. V. (2001). Ice particles in stratiform clouds in the Arctic and possible mechanisms for the production of high ice concentrations. *Journal of Geophysical Research*, *106*, 15065–15075. https://doi.org/10.1029/2000JD900286

Rauber, R. M., Hu, H., Dominguez, F., Nesbitt, S. W., McFarquhar, G. M., Zaremba, T. J., & Finlon, J. A. (2020). Structure of an Atmospheric River over Australia and the Southern Ocean. Part I: Tropical and midlatitude water vapor fluxes. *Journal of Geophysical Research: Atmospheres*, *125*, e2020JD032513. https://doi.org/10.1029/2020JD032513

Schwartz, M. C., Ghate, V. P., Albrecht, B. A., Zuidema, P., Cadeddu, M. P., Vivekanandan, J., et al. (2019). Merged cloud and precipitation dataset from the HIAPER-GV for the Cloud System Evolution in the Trades (CSET) Campaign. *Journal of Atmospheric and Oceanic Technology*, *36*, 921–940. https://doi.org/10.1175/jtech-d-18-0111.1

Smith, W., & Minnis, P. (2018). *NASA SatCORPS Himawari cloud retrieval data*. Version 2.1. UCAR/NCAR - Earth Observing Laboratory. https://doi.org/10.5065/D6CC0ZFJ

Tan, I., Storelvmo, T., & Zelinka, M. D. (2016). Observational constraints on mixed-phase clouds imply higher climate sensitivity. *Science*, *3*, 224–227. https://doi.org/10.1126/science.aad5300

Trenberth, K. E., & Fasullo, J. T. (2010). Simulation of present-day and twenty- first-century energy budgets of the southern oceans. *Journal of Climate*, *23*, 440–454. https://doi.org/10.1175/2009JCLI3152.1

UCAR (2020). *AVAPS dropsondes*. Accessed 30 July 2020. Retrieved from http://www.eol.ucar.edu/content/avaps-dropsondes

Vergara-Temprado, J., Miltenberger, A. K., Furtado, K., Grosvenor, D. P., Shipway, B. J., Hill, A. A., et al. (2018). Strong control of Southern Ocean cloud reflectivity by ice-nucleating particles. *Proceedings of the National Academy of Sciences*, *115*(11), 2687–2692. https://doi.org/10.1073/pnas.1721627115

Vergara-Temprado, J., Murray, B. J., Wilson, T. W., O'Sullivan, D., Browse, J., Pringle, K. J., et al. (2017). Contribution of feldspar and marine organic aerosols to global ice nucleating particle concentrations. *Atmospheric Chemistry and Physics*, *17*, 3637–3658. https://doi.org/10.5194/acp-17-3637-2017

Vivekanandan, J., Ellis, S. M., Tsai, P. S., Loew, E., Lee, W., Emmett, J. M., et al. (2015). A wing pod-based millimeter wavelength airborne cloud radar. *Geoscientific Instrumentation, Methods and Data Systems*, *5*, 117–159. https://doi.org/10.5194/gid-5-117-2015

Welti, A., Bigg, E. K., DeMott, P. J., Gong, X., Hartmann, M., Harvey, M., et al. (2020). Ship-based measurements of ice nuclei concentrations over the Arctic, Atlantic, Pacific and Southern oceans. *Atmospheric Chemistry and Physics*, *20*, 15191–15206. https://doi.org/10.5194/acp-20-15191-2020

Wu, W., & McFarquhar, G. M. (2016). On the impacts of different definitions of maximum dimensions for nonspherical particles recorded by 2D imaging probes. *Journal of Technology*, *33*(5), 1057–1072. https://doi.org/10.1175/JTECH-D-15-0177.1

Wu, W., & McFarquhar, G. M. (2019). *NSF/NCAR GV HIAPER fast 2DS particle size distribution (PSD) product data*. Version 1.1. UCAR/NCAR – Earth observing laboratory. accessed on 03 March 2021. Retrieved from https://doi.org/10.26023/e95a-fkyf-7p0r

Yang, J., Wang, Z., Heymsfield, A. J., DeMott, P. J., Twohy, C. H., Suski, K. J., & Toohey, D. W. (2020). High ice concentration observed in tropical maritime stratiform mixed-phase clouds with top temperatures warmer than −8°C. *Journal of Atmospheric Research*, *233*, 104719. https://doi.org/10.1016/j.atmosres.2019.104719

Zaremba, T. J., Rauber, R. M., McFarquhar, G. M., Hayman, M., Finlon, J. A., & Stechman, D. M. (2020). Phase characterization of cold sector Southern Ocean Cloud tops: Results from SOCRATES. *Journal of Geophysical Research: Atmospheres*, *125*, e2020JD033673. https://doi.org/10.1029/2020jd033673